J Nanopart Res (2019) 21: 203
https://doi.org/10.1007/s11051-019-4652-9

RESEARCH PAPER

A novel Z-scheme Bi_2WO_6-based photocatalyst with enhanced dye degradation activity

Rui Zhang · Tongqing Zhang · Chen Zhao · Qiong Han · Yu Li · Yi Liu · Kunlin Zeng

Received: 13 July 2019 / Accepted: 30 August 2019 / Published online: 9 September 2019

Abstract To overcome the drawback caused by rapid recombination of photogenerated electron-hole pairs, a novel visible-light-driven Bi_2WO_6/r-GO/$Bi_{25}FeO_{40}$ Z-scheme photocatalyst was fabricated through the hydrothermal method. The as-prepared sample was analyzed by X-ray diffraction (XRD), Raman spectroscopy, transmission electron microscopy (TEM), scanning electron microscopy (SEM), electrochemical impedance spectra (EIS), and X-ray photoelectron spectrometer (XPS). At the same time, the photocatalytic performance of ternary material was estimated by degradation of methylene blue (MB) aqueous solution under visible-light irradiation. Bi_2WO_6/r-GO/$Bi_{25}FeO_{40}$ displayed a superior photocatalytic performance compared with pure Bi_2WO_6. A dye degradation rate of 98.1% was appeared in ternary material under a 30-min photocatalytic experiment. r-GO plays an important role in ternary material; it acted as a charge-transfer bridge to accelerate electron transfer from Bi_2WO_6 to $Bi_{25}FeO_{40}$. Therefore, the recombination of the photogenerated electron holes of the Bi_2WO_6 itself was effectively suppressed. Most important, the possible photocatalytic mechanism was evaluated on the basis of UV–vis and PL analysis. This work provides a new idea for the synthesis of new photocatalytic materials with enhanced photocatalytic properties.

Keywords Bi_2WO_6/r-GO/$Bi_{25}FeO_{40}$ · Z-Scheme · Visible-light photocatalyst · Nanostructured catalysts

R. Zhang · T. Zhang (✉) · C. Zhao · Q. Han · Y. Li · Y. Liu · K. Zeng
Southwest Petroleum University, Chengdu, Sichuan Province, China
e-mail: 1456765395@qq.com

R. Zhang
e-mail: 2482854366@qq.com

C. Zhao
e-mail: 987005283@qq.com

Q. Han
e-mail: 1032841867@qq.com

Y. Li
e-mail: 772733709@qq.com

Y. Liu
e-mail: 1034028266@qq.com

K. Zeng
e-mail: 997026364@qq.com

Introduction

Methylene blue (MB), a water-soluble polycyclic aromatic hydrocarbon, is commonly used in industrial, pharmaceutical, aquaculture, and skin care areas (Liu et al. 2012). However, causing serious pollution to water due to increased production and wide application, the polluted water with MB has the characteristics of high concentration, high chroma, high pH, and hard to degradation (Saravanan et al. 2013). Researchers have tried many methods to solve the above problem, such as

adsorption, photocatalytic technology, and membrane separation technology; photocatalytic technology has been widely concerned owing to its low energy consumption, mild conditions, simple operation, and no secondary pollution.

Over the past few decades, Bi_2WO_6, a typical narrow band gap semiconductor ($E_g \approx 2.7$ eV), has been widely used for photodegradation of organic contaminants due to its unique structure and stable chemical properties (And and Zhu 2010). However, the photoactivity of pure Bi_2WO_6 is still not satisfactory attributing to the rapid recombination of photogenerated electron-hole pairs, so designing a new photocatalyst to improve its photocatalytic efficiency is imperative. Heterostructure photocatalyst has been proved to be a good choice to enhance the photocatalytic performance in comparation to single-component photocatalyst, with successful cases like Fe_3O_4/Bi_2WO_6 (Zhou et al. 2015), Cd/Bi_2WO_6 (Xu et al. 2015), $AgBr/Ag/Bi_2WO_6$ (Zhang et al. 2009), $g\text{-}C_3N_4/Bi_2WO_6$ (Lei et al. 2011), Bi_2S_3/Bi_2WO_6 (Sangeeta and Do-Heyoung 2018), and CdS/Bi_2WO_6 (Lei GE, Liu J 2011). These composite materials display an enhanced photocatalytic performance owing to the fast transfer photogenerated electrons-hole pair.

$Bi_{25}FeO_{40}$, a typical soft bismuth ore material, with a relatively narrow band gap (2.1–2.7 eV) (Ji et al. 2017), has been regarded as a promising photocatalyst attributing to its special structure, a crystal structure with a large number of oxygen vacancies and ion vacancies, which can greatly improve the photocatalytic performance of material (Köferstein et al. 2014). Unfortunately, the photocatalytic performance of pure $Bi_{25}FeO_{40}$ can only be enhanced by the addition of an electron scavenger such as H_2O_2, which can surpass the recombination of photogenerated electrons-hole pairs (Wisedsri et al. 2011; Hou et al. 2010). Until now, researchers have been tried many ways to improve its photocatalytic performance, such as $Bi_{25}FeO_{40}$/RGO (Basith et al. 2018), $Bi_{25}FeO_{40}/Bi_2Fe_4O_9$ (Wang et al. 2019), and $Bi_{25}FeO_{40}/Fe_3O_4/Fe_2O_3$ (de Góis et al. 2019). In light of this, the emergence of an all-solid-state Z-scheme heterojunction could address the problem to some extent. In this Z-scheme system, the photogenerated electrons in the CB of PSII could recombine with the holes in the VB of PSI; thus, holes with strong oxidizing ability are left in the VB of PSII and photogenerated electrons with strong reducing ability are left in the CB of PSI(Hu et al. 2017; Zhou et al. 2014). Also, conductive medium plays an important role in Z-scheme system, like Au (Bai et al. 2016), Ag (Li et al. 2017), and graphene oxide (GO) (Jiang et al. 2017; Miao et al. 2017; Rakibuddin et al. 2017) or reduced graphene oxide (r-GO) (Li et al. 2014; Jo and Selvam 2017; Chen et al. 2017); among them, r-GO stands out due to its large specific surface area and strong electrical conductivity. Ma et al. (2016) fabricated a Z-scheme catalyst named $g\text{-}C_3N_4/r\text{-}GO/Bi_2WO_6$; the excellent photocatalytic performance had been verified by degrading TCP. Zhang et al. (2016a, b) constructed a $Bi_2WO_6/MoS_2/RGO$ Z-scheme catalyst to remove Cr^{6+}; the r-GO could effectively improve the photocatalytic performance of Bi_2WO_6. Wu et al. (2017) synthesized a $g\text{-}C_3N_4\text{-}r\text{-}GO\text{-}TiO_2$ Z-scheme system and further revealed the multi-functional roles of r-GO in enhancing the photodegradation rate.

In summary, a novel Z-scheme photocatalyst $Bi_2WO_6/r\text{-}GO/Bi_{25}FeO_{40}$ was fabricated, and Bi_2WO_6 ($E_{CB} = +0.6$ V, $E_{VB} = +3.26$ V vs. NHE) and $Bi_{25}FeO_{40}$ ($ECB = -1.3$ V, $E_{VB} = +1.13$ V vs. NHE) were matched well. Firstly, nanosheet Bi_2WO_6 was synthesized in the presence of CTAB, then Bi_2WO_6 was used as a precursor template, and $Fe(NO_3)_3{\cdot}9H_2O$ and r-GO were added to obtain a ternary material under hydrothermal condition of 180 °C. The photocatalytic performance was evaluated by degrading RhB solution under visible-light irradiation. Ternary material exhibited better photocatalytic performance than binary and single materials. At the same time, a possible photodegradation mechanism of $Bi_2WO_6/r\text{-}GO/Bi_{25}FeO_{40}$ has been discussed in detail on the basis of UV–vis and PL results. Such distinctive Z-scheme photocatalyst has greatly overcome the shortcomings of Bi_2WO_6 and successfully achieved the separation of photogenerated electron-hole pairs.

Experiment

Materials

All reagents used in this experiment were of analytical grade and were not further purified prior to use. All of them were purchased from Chengdu Kelong Co., Ltd.

Preparation of Bi_2WO_6 nanosheet

The nanosheet Bi_2WO_6 was constructed through the hydrothermal method. Typically, 1.2125 g of

$Bi(NO_3)_3{\cdot}5H_2O$ and 0.1 g of hexadecyl trimethyl ammonium bromide (CTAB) were firstly dispersed into 50 mL of deionized water under ultrasonic treatment until obtaining a clear solution, subsequently adding 0.4125 g of $Na_2WO_4{\cdot}2H_2O$ to above solution and keeping vigorous magnetic stirring at room temperature for 30 min. Transferring the mixed solution to a 100-mL Teflon-lined autoclave and keeping at 160 °C for 12 h. The precipitate was washed with ethanol and deionized water for several times after completion of the hydrothermal reaction. Bi_2WO_6 nanosheet was obtained after drying at 60 °C for 12 h.

Preparation of $Bi_{25}FeO_{40}$, $Bi_2WO_6/Bi_{25}FeO_{40}$, and Bi_2WO_6/r-GO/$Bi_{25}FeO_{40}$

At first, graphene oxide (GO) was fabricated through modified Hummer's method (Shi et al. 2016). Then, 0.5 g of Bi_2WO_6 was dispersed in deionized water, followed by a certain amount of $Fe(NO_3)_3{\cdot}9H_2O$ was added to the above solution, adjusting the pH of the solution to 10 using NaOH solution (10 M). In addition, 10 mg of GO and 1 mg of L(+)-ascorbic acid (L-AA) were dissolved in 10 mL of deionized water and ultrasonicated for 30 min to obtain even solution, mixing the above two solutions and stirring for 1 h, then transferring the mixed solution to a 100-mL Teflon-lined autoclave, and keeping at 180 °C for 12 h. The precipitate was washed with ethanol and deionized water for several times after the hydrothermal reaction was completed. Ternary material was obtained after drying at 100 °C for 10 h. For comparison, the pristine $Bi_{25}FeO_{40}$ and $Bi_2WO_6/Bi_{25}FeO_{40}$ were prepared under identical condition without adding Bi_2WO_6 or GO.

Characterization

The crystalline phases and purity of catalysts were determined by an X-ray diffractometer (XRD, PANalytical B.V., X Pert PRO MPD) with a Cu-Kα radiation (λ = 1.54060 Å, 40 kV, 40 mA) in the range of $5° \le 2\theta \le 80°$, operated at a scanning rate of 1°/min. Raman spectra (Oceanoptics, IDRaman micro IM-52) was used to analyze the molecular structure of materials. The morphology structures, element composition, and distribution of as-prepared samples were observed by scanning electron microscopy (SEM, Carl Zeiss AG, ZEISS EV0 MA15) equipped with an energy dispersive X-ray (EDX) spectroscopy. The nanostructures of catalysts were tested using a transmission electron microscope (TEM, Japan, Jeol 2100F). The UV–vis absorption spectra were recorded by a UV–vis spectrometer (Platinum Elmer Instrument Co., Ltd., PerkinEImerLambda850), choosing $BaSO_4$ as background. The surface chemical composition and chemical states of solid surface were carried out using an X-ray photoelectron spectrometer (XPS, America, Thermo ESCALAB 250XI) with Al Kα source. Photoluminescence (PL) spectra of samples were implemented using a PerKinEImer LS55 spectrofluorometer with an excitation wavelength of 270 nm.

Electrochemical measurements

The electrochemical impedance spectra (EIS) and photocurrent response intensity curve were obtained through CHI604D (Shanghai) electrochemical workstation equipped with a standard three-electrode cell: A Pt counter electrode, a saturated calomel reference electrode, and a FTO glass working electrode in the experiment; the electrolyte is Na_2SO_4 aqueous solution (0.5 M) and a 200 W LED lamp is used as a light source. Specific steps are as follows: a 5 mg of sample was dissolved in a mixed solution consisting of 50 μL of 5% Nafion solution and 1 mL absolute ethanol, and then ultra-sonicated for 30 min to obtain a uniform solution. The suspension was coated on the FTO glass working electrode to make an effective exposed area of 1 cm^2, measuring after ventilation overnight.

Photocatalytic experiment

The photocatalytic performance of all samples was evaluated by degrading MB aqueous solution under visible-light irradiation. There are same steps in each sample: 40 mg of the photocatalyst was dispersed into 50 mL of MB aqueous solution (20 mg/L). Before lighting, the mixed solution was stirred for 30 min in dark to ensure good dispersion and establish an adsorption–desorption equilibrium and then exposed to 200 W of visible light to begin photocatalytic experiment. The solution of aliquots volume was centrifuged to remove photocatalytic powders every 5 min, and then, the concentration of MB molecule at different time was measured by a UV–visible spectrophotometer (UV-1800, Shimadzu, Japan) at $\lambda = 664$ nm; deionized water was reference solution. Generally, calculating the degradation rate by

the following formula: $\eta = \frac{C_0 - C_t}{C_0} \times 100\%$, where C_0 is the initial concentration of MB and C_t is the concentration of MB at time t (min). In addition, cyclic stability of photocatalytic material is a critical performance too, which was recycled four times to ensure its reliability. The photocatalytic powders were washed with deionized water and ethanol for several times at the end of each experiment, and then, put it in fresh MB solution to start next recycle under identical condition.

Results and discussion

Crystal structure and morphology

The XRD patterns of GO, Bi_2WO_6, $Bi_{25}FeO_{40}$, $Bi_2WO_6/Bi_{25}FeO_{40}$, and Bi_2WO_6/r-GO/$Bi_{25}FeO_{40}$ are shown in Fig. 1. The characteristic peak located at $2\theta = 9.6°$ in the GO XRD pattern is assigned to the (001) plane of GO (Zhu et al. 2018). For pure Bi_2WO_6, the conspicuous peaks located at $2\theta = 28°$, 34°, 47.5°, 56°, 59°, 69°, 76°, and 79° are assigned to (113), (006), (220), (313), (226), (400), (139), and (420) respectively (Zhang et al. 2016a, b). The sharp peak patterns of Bi25FeO_{40} are in good assignment with the standard Joint Committee on Powder Diffraction Standards (JCPDS); the peaks at 24°, 27°, 30°, 33°, 39°, 52°, 66°, and 78° are related to (220), (310), (222), (321), (332), (530), (640), and (653) respectively (Zhang et al. 2015). However, the charactiristic peaks of Bi_{25} FeO_{40} have been not found in binary composite and ternary composite, only the charactiristic peaks of Bi_6 WO_6 appeared. Probably because the small dosage of $Fe(NO_3)_3 \cdot 9H_2O$ (6% by Bi_2WO_6) is wrapped with Bi_2WO_6 to make it difficult to detect. Also, the characteristic peak of GO in the XRD pattern of Bi_2WO_6/r-GO/$Bi_{25}FeO_{40}$ cannot be appeared, which can be considered as the relatively low amount of GO and the appearance of RGO. No other impurity phases appear, proving the high purity of Bi_2WO_6/r-GO/$Bi_{25}FeO_{40}$.

To discuss the morphology and detailed structure of as-prepared products, SEM images are displayed in Fig. 2a–c. The pure Bi_2WO_6 is constructed from a large number of regular square nanosheets. GO displays a flake-like structure with a wrinkled surface (Fig. 2b). For Bi_2WO_6/r-GO/$Bi_{25}FeO_{40}$ (Fig. 2c), the r-GO and $Bi_{25}FeO_{40}$ do not cover the square structure of Bi_2WO_6 due to the small dosage. The $Bi_{25}FeO_{40}$ particles load on the Bi_2WO_6 square nanosheet, and they are in close contact with r-GO, which can promote the effective separation of photogenerated electron-hole pairs and further improve the photocatalytic activity of ternary composite. Moreover, the EDS pattern suggests that there are five elements of Bi, W, Fe, O, and C in the ternary composite. In addition, TEM technology is operated to further characterize the morphology of Bi_2WO_6 and Bi_2WO_6/r-GO/$Bi_{25}FeO_{40}$. As shown in

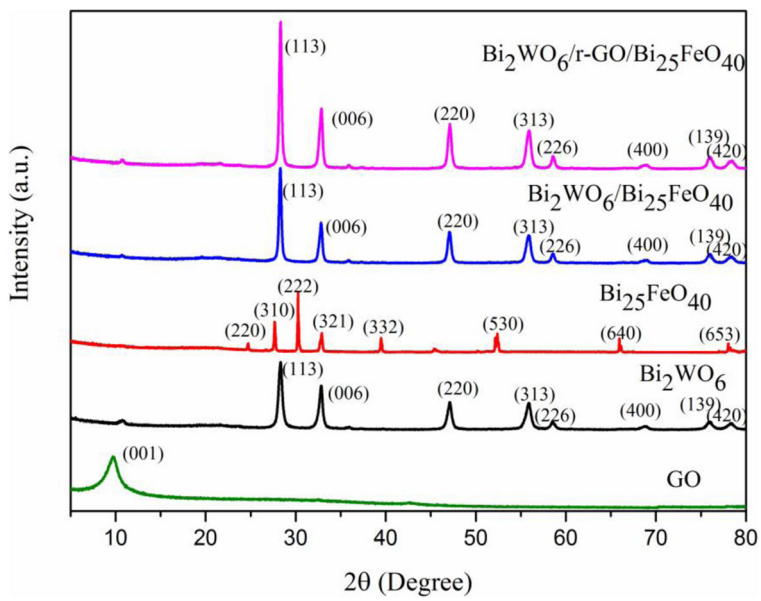

Fig. 1 XRD patterns of GO, Bi_2WO_6, $Bi_{25}FeO_{40}$, $Bi_2WO_6/Bi_{25}FeO_{40}$, and Bi_2WO_6/r-GO/$Bi_{25}FeO_{40}$ composites

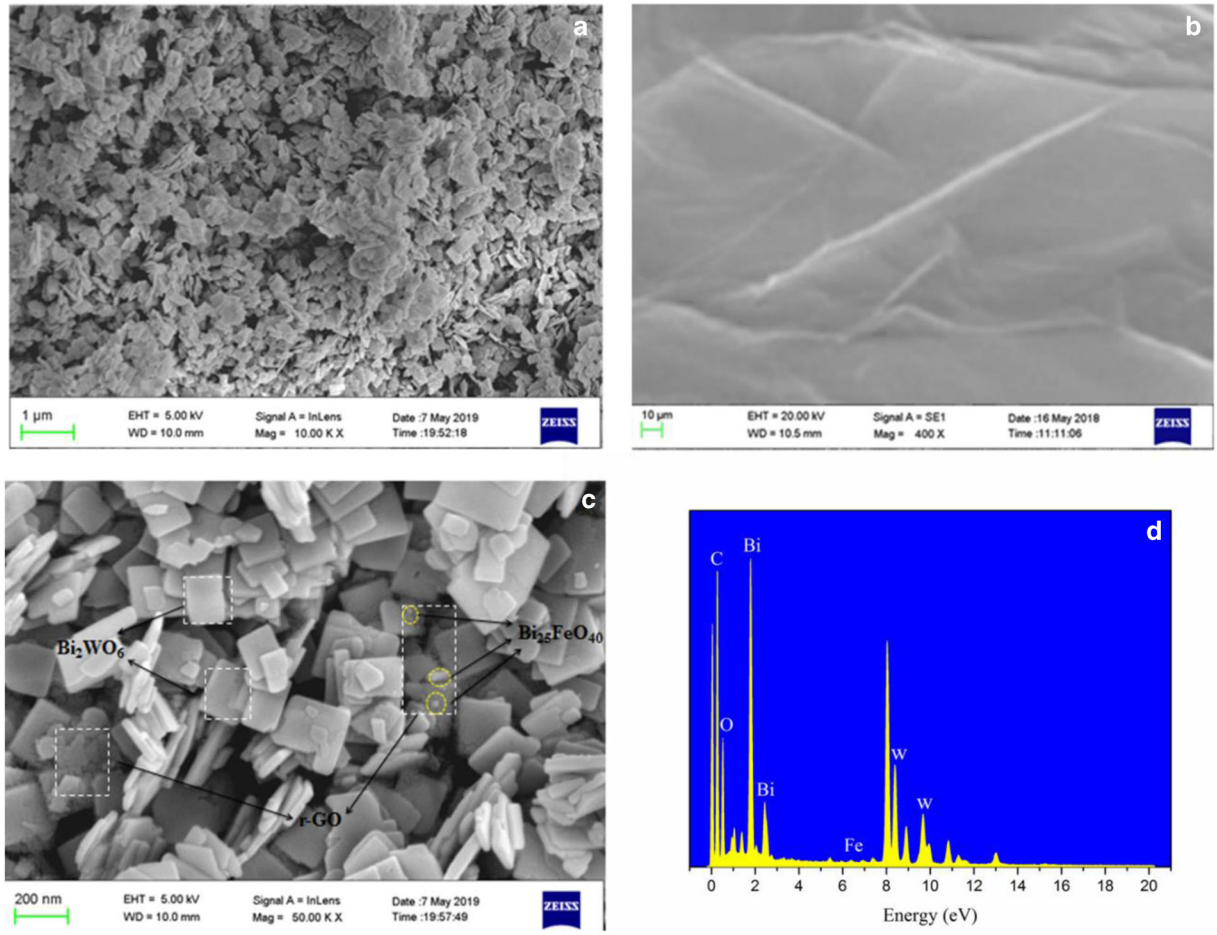

Fig. 2 SEM images of **a** Bi_2WO_6, **b** GO, and **c** Bi_2WO_6/r-GO/$Bi_{25}FeO_{40}$, and the EDS pattern of **d** Bi_2WO_6/r-GO/$Bi_{25}FeO_{40}$

Fig. 3a, Bi_2WO_6 has a square structure. The ternary composite reveals an irregular morphology after the introduction of r-GO and $Bi_{25}FeO_{40}$, which is in agreement with SEM analysis that $Bi_{25}FeO_{40}$, Bi_2WO_6, and r-GO are in good contact with each other.

Surface structure and properties

Raman spectroscopy was employed to provide further evidence of the local structure of materials. As shown in Fig. 4, the Raman peaks at approximately 304, 712, and

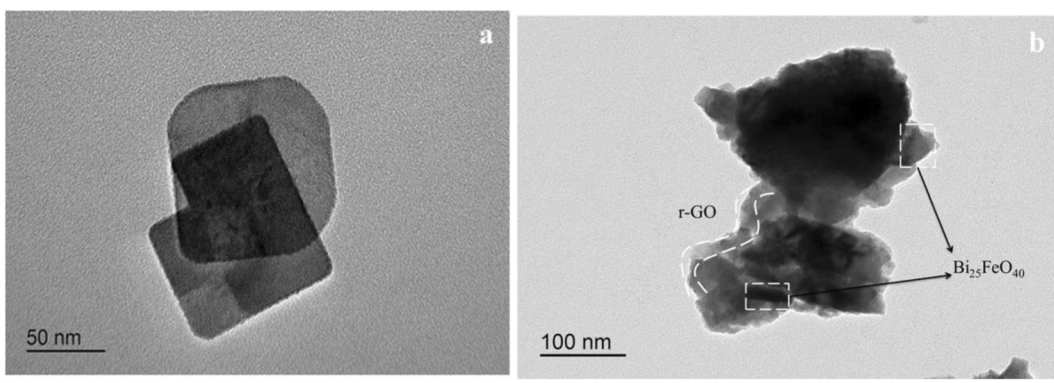

Fig. 3 TEM images of **a** Bi_2WO_6 and **b** Bi_2WO_6/r-GO/$Bi_{25}FeO_{40}$

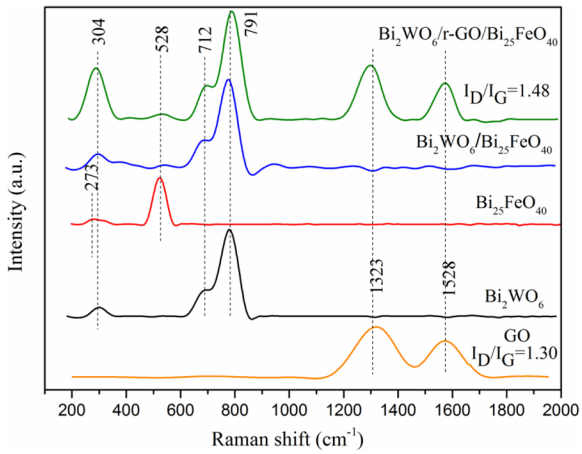

Fig. 4 Raman spectra of GO, Bi_2WO_6, $Bi_{25}FeO_{40}$, Bi_2WO_6/$Bi_{25}FeO_{40}$, and Bi_2WO_6/r-GO/$Bi_{25}FeO_{40}$ composites

791 cm^{-1} were appeared in pure Bi_2WO_6 which were in assignment with the bending vibration of WO_6, antisymmetric bridging mode of tungstate chains, and stretching vibration (Ma et al. 2016). For single $Bi_{25}FeO_{40}$, the peaks mainly concentrate on 273 and 528 cm^{-1}. Two distinct peaks at 1323 and 1528 cm^{-1} are related to D (the symmetry A1g k-point phonon) and G (the E2g phonon of sp2 carbon atoms) bands of GO (Chen et al. 2017). In general, the intensity ratio (I_D/I_G) of the D band and the G band can indicate the reduction degree of GO (Shen et al. 2017), the larger the I_D/I_G, the higher the reduction degree of GO. Similarly, the characteristic peaks of GO and Bi_2WO_6 in the Raman spectra are clearly visible; however, the peaks of $Bi_{25}FeO_{40}$ are indistinguishable, indicating that $Bi_{25}FeO_{40}$ is highly dispersed on the surface of ternary composite. Furthermore, the value of I_D/I_G (1.48) in Bi_2WO_6/r-GO/$Bi_{25}FeO_{40}$ is increased compared with GO (I_D/I_G = 1.30), indicating successful reduction of GO during the hydrothermal process.

The chemical states of the ternary composite are studied by means of XPS technique. As the full survey spectra of Bi_2WO_6/r-GO/$Bi_{25}FeO_{40}$ are shown in Fig. 5a, the signals of Bi, W, Fe, O, and C elements are found in ternary composite, indicating the presence of Bi_2WO_6, $Bi_{25}FeO_{40}$, and r-GO. Figure 5 b exhibits the Bi 4f spectra of ternary composite in which the peaks at 159.4 and 164.7 eV are assigned to Bi $4f_{7/2}$ and Bi $4f_{5/2}$ respectively, suggesting that the elemental state of bismuth is Bi^{3+} (Wu et al. 2007) in the catalyst. For the XPS result of Fe 2p, the signal has been divided into Fe $2p_{1/2}$ and Fe $2p_{3/2}$ attributing to the spin–orbit coupling (Zhang et al. 2016a, b), the peak centers located at 709.8 and 723.4 eV respectively. Figure 5 d shows the XPS result of W; the two typical peaks at 35.78 and 37.9 eV are assigned to W $4f_{7/2}$ and W $4f_{5/2}$, which can be ascribed to the oxidation state of W^{6+} (Fu et al. 2005). As shown in Fig. 5e, the characteristic orbital of the O 1s is observed with peak locations at 531.9, 529.8, and 531.0 eV, which are corresponding to the r-GO (Zhu et al. 2018), Fe–O–Bi, and Bi–O–W (Zhang et al. 2016a, b). The binding energy peaks in Fig. 5f at 284.9, 286.8, 287.7, and 288.7 eV are well in accordance with C 1s state in r-GO, which are assigned to C–C, C–O, C=O, and O–C=O (Zhu et al. 2018) respectively. All binding energies are consistent with previous reports.

The optical absorption properties of as-prepared samples are investigated via the UV–vis DRS technique. All samples exhibit visible-light absorption in the wavenumber range of 200 to 700 cm^{-1} in Fig. 6. Ternary composite establishes a wide absorption edge after the introduction of $Bi_{25}FeO_{40}$ and r-GO; the absorption edges of Bi_2WO_6, $Bi_{25}FeO_{40}$, Bi_2WO_6/$Bi_{25}FeO_{40}$, and Bi_2WO_6/r-GO/$Bi_{25}FeO_{40}$ are 470, 520, 610, and 680 cm^{-1} respectively, indicating the ternary material can make full use of visible light and further improve the photocatalytic performance. Meanwhile, the band gap energy is calculated according to the following formula:

$$(\alpha h\nu)^n = A\left(h\nu - E_g\right)$$

where α, ν, A, and E_g are absorption coefficient, optical frequency, constant, and band gap respectively; the value of n depends on the type of semiconductor; there is 1/2 in direct band gap and 2 in indirect band gap (López and Gómez 2012). The value of n in Bi_2WO_6 and $Bi_{25}FeO_{40}$ are both 2 due to they are indirect gap semiconductor. As shown in Fig. 3, the band gap of Bi_2WO_6 and $Bi_{25}FeO_{40}$ is 2.66 and 2.42 eV respectively, which are similar to previous reports.

Photoelectrochemical performance

The electrochemical impedance spectroscopy (EIS) test is an effective method for analyzing the separation efficiency of photogenerated electron-hole pairs. Generally, the smaller the arc radius of the EIS diagram, the higher the photogenerated electron-hole pairs separation efficiency (Shi et al. 2016). As shown in Fig. 7a, the arc radius of all samples is in the order $Bi_{25}FeO_{40}$ > Bi_2WO_6 > Bi_2WO_6/$Bi_{25}FeO_{40}$ > Bi_2WO_6/r-GO/$Bi_{25}FeO_{40}$ composites. Obviously,

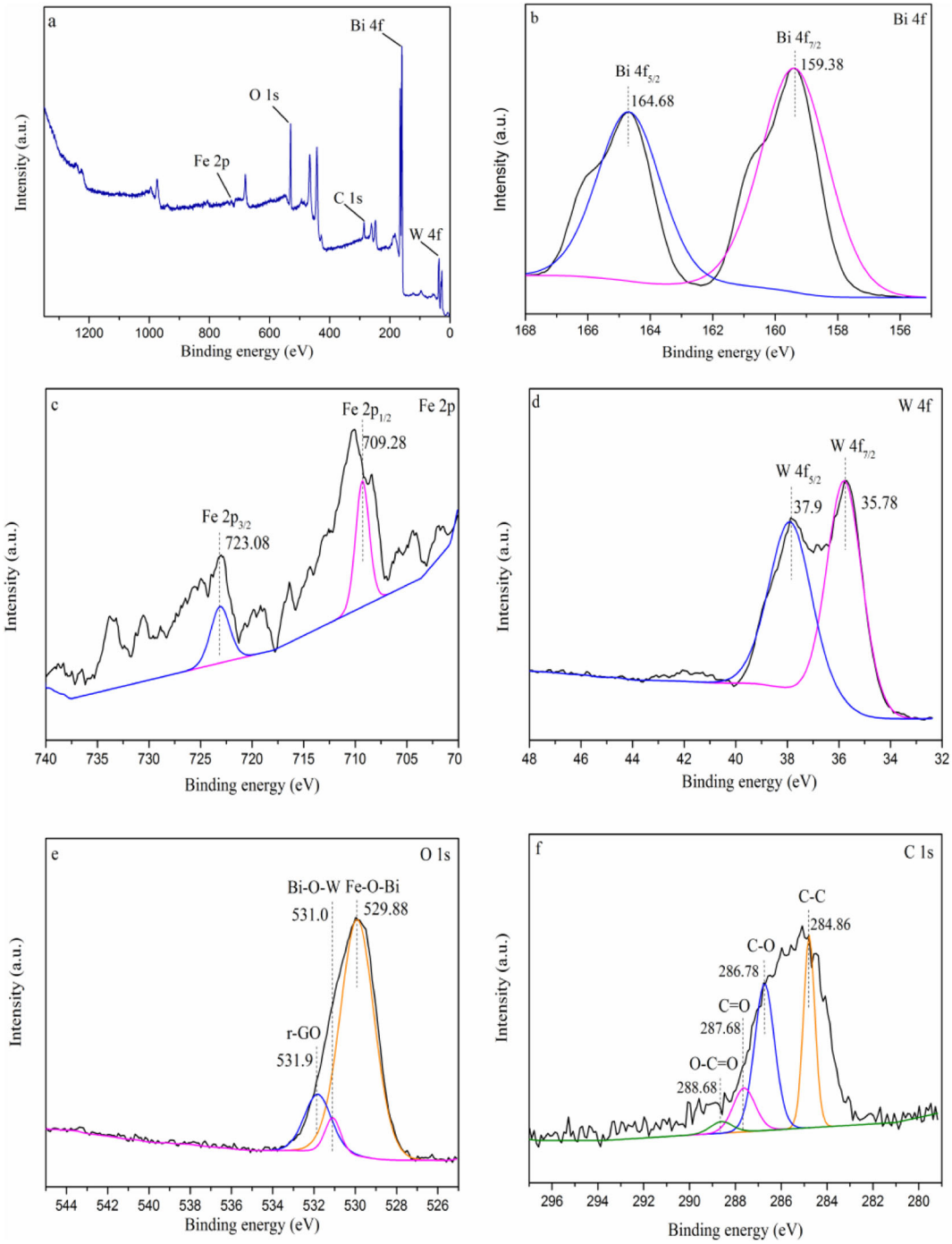

Fig. 5 XPS spectra of Bi_2WO_6/r-GO/$Bi_{25}FeO_{40}$ composite, **a** survey, **b** Bi 4f, **c** Fe 2p, **d** W 4F, **e** O 1s, and **f** C 1s

ternary material with the smallest arc radius has the highest photogenerated electron-hole pairs' separation efficiency, which is consistent with the PL response. The photocurrent response intensity curve of all samples was conducted to the same electrolyte (Na_2SO_4 solution, 0.5 M) under the condition of alternating light and dark. As seen in Fig. 7b, modified Bi_2WO_6/r-GO/$Bi_{25}FeO_{40}$ exhibits a higher photocurrent response intensity than single Bi_2WO_6; its value can reach 2.38 μA/cm^2 which is about 6.4 times than

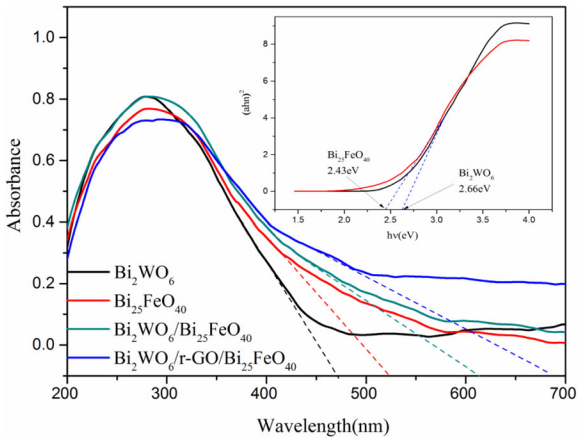

Fig. 6 UV–vis DRS spectra of Bi_2WO_6, $Bi_{25}FeO_{40}$, and the $Bi_2WO_6/Bi_{25}FeO_{40}$ and Bi_2WO_6/r-GO/$Bi_{25}FeO_{40}$ composites, and the plot of $(\alpha h\nu)^2$ vs. hν (inset) for Bi_2WO_6 and $Bi_{25}FeO_{40}$

that of pristine Bi_2WO_6. Such Z-scheme photocatalyst will show excellent potential in water treatment and other fields.

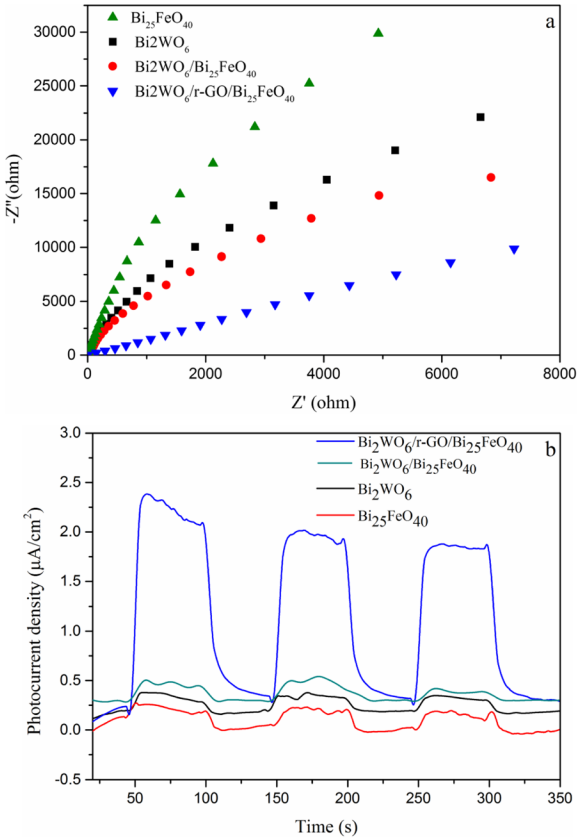

Fig. 7 **a** EIS Nyquist plots and **b** photocurrent response spectra of Bi_2WO_6, $Bi_{25}FeO_{40}$, and the $Bi_2WO_6/Bi_{25}FeO_{40}$ and Bi_2WO_6/r-GO/$Bi_{25}FeO_{40}$ composites

Photocatalytic degradation of RhB

The photoluminescence (PL) spectra are investigated to evaluate the migration and recombination processes of photogenerated electrons-hole pairs of the photocatalyst. Fluorescence comes from the recombination of free carriers inside the semiconductor, the faster the recombination of photogenerated electron-hole pairs, the higher the fluorescence excitation intensity of the material. As shown in Fig. 8, the emission peaks of all samples focus on 450 nm; Bi_2WO_6 exhibits a strong PL intensity owing to the rapid recombination of photogenerated electron-hole pairs on its surface. The PL strength of $Bi_2WO_6/Bi_{25}FeO_{40}$ is lower than that of Bi_2WO_6 and $Bi_{25}FeO_{40}$, indicating the combination of the two can suppress the recombination of photogenerated electron-hole pairs. More importantly, Bi_2WO_6/r-GO/$Bi_{25}FeO_{40}$ displays a weaker PL intensity than $Bi_2WO_6/Bi_{25}FeO_4$, revealing r-GO as an electronic modifier in the Bi_2WO_6/r-GO/$Bi_{25}FeO_{40}$ enables higher separation of photogenerated electron-hole pairs, and then, more active substances generated in the photocatalytic process. The result indicates the successful construction of Z-scheme photocatalyst.

To demonstrate the photocatalytic activity of all samples, the photodegradation of MB aqueous solution (20 mg/L) was operated under visible-light irradiation at room temperature. The dynamic degradation curve of all samples is shown in Fig. 9a. Bi_2WO_6/r-GO/$Bi_{25}FeO_{40}$ displays superior photocatalytic performance in 30-min irradiation compared with pure Bi_2WO_6. Furthermore, the blank experiment without photocatalyst

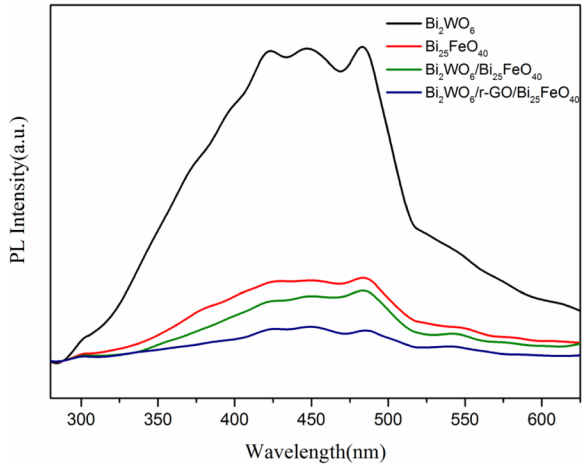

Fig. 8 Photoluminescence spectra for pure Bi_2WO_6, $Bi_{25}FeO_{40}$, $Bi_2WO_6/Bi_{25}FeO_{40}$, and Bi_2WO_6/r-GO/$Bi_{25}FeO_{40}$ composites

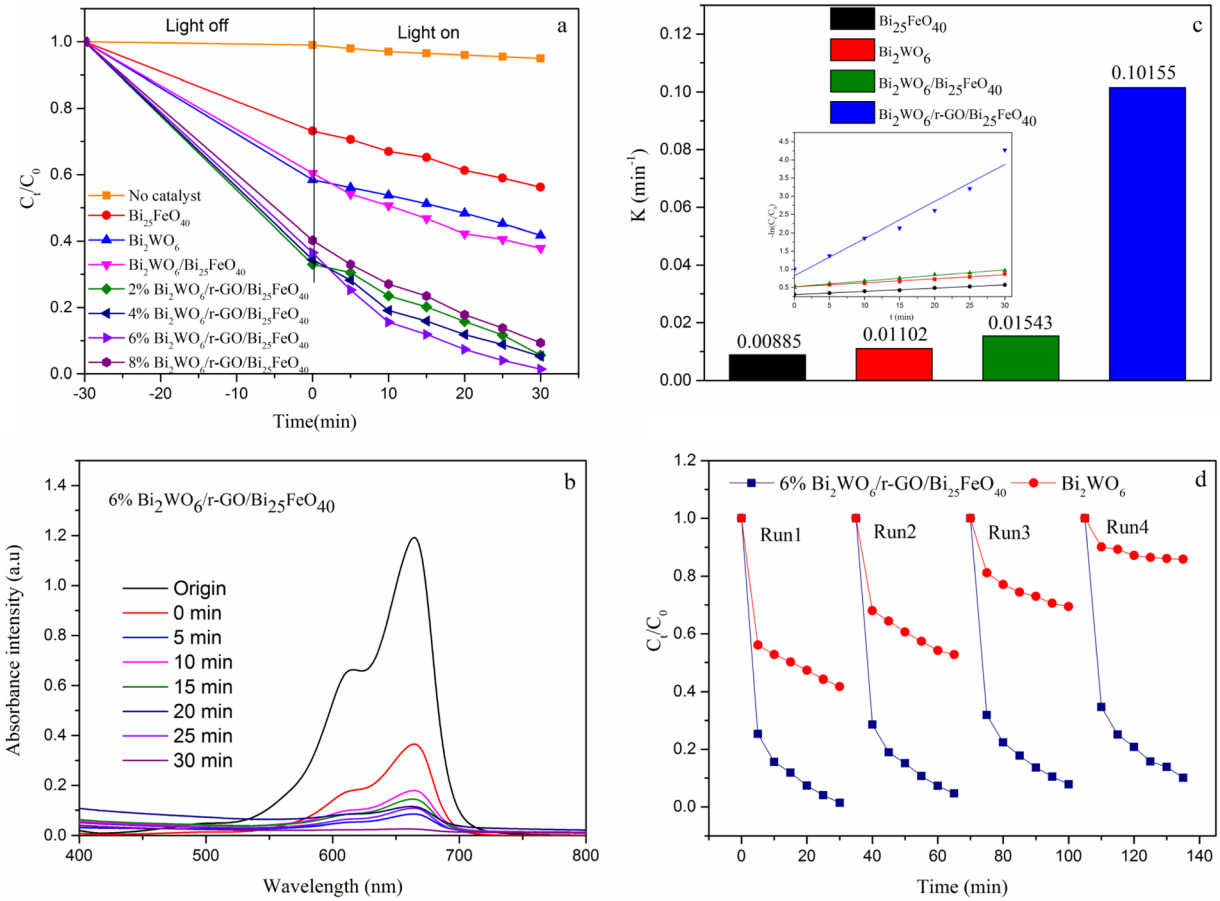

Fig. 9 **a** Dynamic degradation curve of MB with different catalysts under visible-light irradiation. **b** Absorption changes of MB solution in the presence of 6% Bi_2WO_6/r-GO/$Bi_{25}FeO_{40}$ composite. **c** Reaction rate constants (k) of the as-prepared samples. **d** Cycling performances of photocatalytic degradation of MB over Bi_2WO_6 and Bi_2WO_6/r-GO/$Bi_{25}FeO_{40}$

proves that the property of MB is stable, thus the self-photolysis of it can be ignored. The degradation rate of Bi_2WO_6/r-GO/$Bi_{25}FeO_{40}$ is close to 98.1% that is about 2.3 times than that of pure Bi_2WO_6 (42%). Furthermore, the UV–vis absorption spectrum of Bi_2WO_6/r-GO/$Bi_{25}FeO_{40}$ is shown in Fig. 9b, which further explains the change in MB concentration during the irradiation time. In addition, the kinetic of the photocatalytic reaction is in line with first-order reaction that can be described as: $\ln(C_t/C_0) = kt$. Here, C_0 is the initial concentration of MB, C_t is the concentration of MB at irradiation time t (min), and k (min^{-1}) is apparent reaction rate constant. Obviously, Bi_2WO_6/r-GO/$Bi_{25}FeO_{40}$ shows a highest reaction rate constant (0.10155 min^{-1}) which is about 9.2 and 11.4 times than that of Bi_2WO_6 and $Bi_{25}FeO_{40}$, respectively. Meanwhile, the stability of Bi_2WO_6 and Bi_2WO_6/r-GO/$Bi_{25}FeO_{40}$ was studied via recycling experiment; all conditions are the same as mentioned above. The catalyst was centrifuged and washed with deionized water at the end of each cycle. It is obvious that Bi_2WO_6/r-GO/$Bi_{25}FeO_{40}$ exhibits a better stability than Bi_2WO_6 after four cycles.

Photocatalytic mechanism

In order to clearly elaborate the possible degradation mechanism of Bi_2WO_6/r-GO/$Bi_{25}FeO_{40}$, the Mott–Schottky plots and UV–vis spectra were carried out to estimate the CB and VB potentials of Bi_2WO_6 and $Bi_{25}FeO_{40}$. As shown in Fig. 10, the flat band potential (U_{fb}) values of Bi_2WO_6 and $Bi_{25}FeO_{40}$ are + 0.56 and − 1.34 V (vs. SCE). Then, the values of CB are 0.36 and − 1.54 V (vs. SCE, CB ≈ U_{fb} − 0.2 V), and they are 0.6 and − 1.3 V vs. normal hydrogen electrode (NHE, NHE = SCE + 0.24 V) (Xu et al. 2018). In addition, the VB potentials of Bi_2WO_6 and $Bi_{25}FeO_{40}$ could

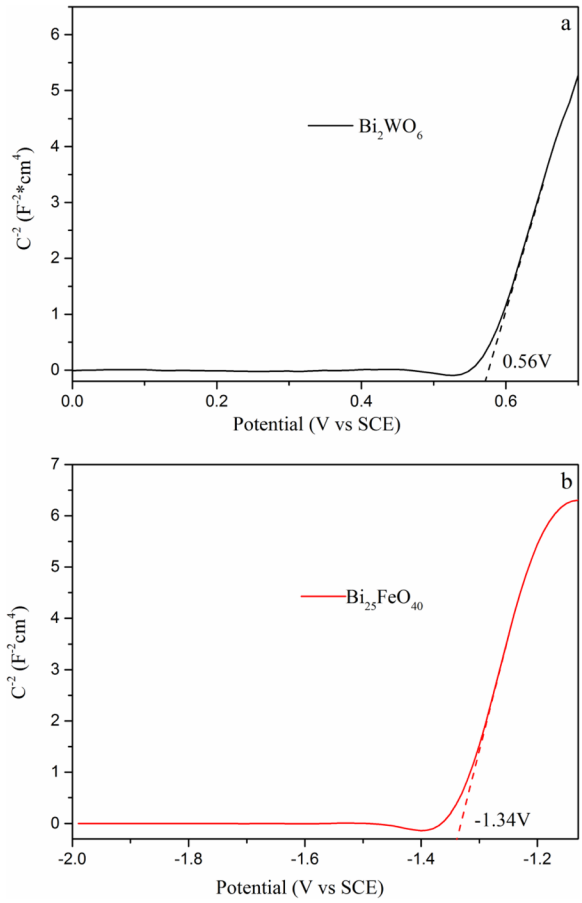

Fig. 10 Mott–Schottky plots of Bi_2WO_6 (**a**) and $Bi_{25}FeO_{40}$ (**b**)

calculate through $E_{VB} = E_{CB} + E_g$ (Lin et al. 2017), and the E_g values for Bi_2WO_6 and $Bi_{25}FeO_{40}$ are 2.66 and 2.43 V according to UV–vis results. Therefore, the VB potentials of Bi_2WO_6 and $Bi_{25}FeO_{40}$ are determined to be 3.26 and 1.13 V. The band structures of them are shown in Fig. 11.

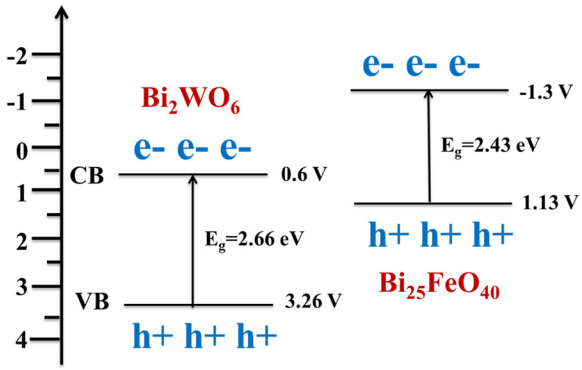

Fig. 11 Energy band structure of Bi_2WO_6 and $Bi_{25}FeO_{40}$

Zhang et al. (2016a, b) had analyzed the double transfer theory of $Bi_2WO_6/Bi_{25}FeO_{40}$. The photogenerated electrons in the CB of $Bi_{25}FeO_{40}$ transfer to the VB of Bi_2WO_6, while the holes deposited on VB of $Bi_{25}FeO_{40}$ and electrons were left at CB of Bi_2WO_6. The photogenerated electrons and holes are effectively separated to improve the photocatalytic performance of the material. It is obvious that the double transfer theory cannot explain the mechanism of Bi_2WO_6/r-GO/$Bi_{25}FeO_{40}$ in MB dye degradation under visible light. So, we propose the Z-scheme mechanism of Bi_2WO_6/r-GO/$Bi_{25}FeO_{40}$ followed the previous reports and illustrated in Fig. 12. The band gap of Bi_2WO_6 and $Bi_{25}FeO_{40}$ is 2.66 and 2.43 eV respectively, while the CB and VB potentials of Bi_2WO_6 are estimated to be + 0.6 and + 3.26 eV, and for $Bi_{25}FeO_{40}$, they are − 1.3 and 1.13 eV. As shown in Fig. 12, after irradiated with visible light, the photogenerated electrons in the CB of Bi_2WO_6 could rapidly transfer to the VB of $Bi_{25}FeO_{40}$ through r-GO and recombine with holes, and the remaining photogenerated electrons and holes are accumulated on the CB of $Bi_{25}FeO_{40}$ and the VB of Bi_2WO_6, respectively. Notably, the CB potential (− 1.3 eV) on $Bi_{25}FeO_{40}$ is more negative than that of $O_2/{}^{\cdot}O_2^-$ (− 0.46 eV) (Wu et al. 1998), which can reduce O_2 to ${}^{\cdot}O_2^-$ radicals. Meanwhile, the VB potential (3.26 eV) on Bi_2WO_6 is more positive than that of $H_2O/{}^{\cdot}OH$ (2.85 eV) (Li et al. 2015), thus the H_2O could be oxidized to ${}^{\cdot}OH$, and the holes with excellent oxidation ability on VB can directly degrade the dye in the photocatalytic process. r-GO plays two important roles in this photocatalytic system, on the one hand, increasing the contact area and reaction space between catalyst and contaminant, and, on the other hand, accelerating the transfer of electrons between Bi_2WO_6 and $Bi_{25}FeO_{40}$, effectively suppressing the recombination of photogenerated electron-hole pairs. In summary, the photocatalytic activity of Bi_2WO_6/r-GO/$Bi_{25}FeO_{40}$ is greatly improved. In addition, the photocatalytic process of Bi_2WO_6/r-GO/$Bi_{25}FeO_{40}$ Z-scheme can be described as follows:

$$Bi_2WO_6 + h\nu \rightarrow Bi_2WO_6(e^- + h^+)$$
$$Bi_{25}FeO_{40} + h\nu \rightarrow Bi_{25}FeO_{40}(e^- + h^+)$$
$$Bi_2WO_6(e^- + h^+) + Bi_{25}FeO_{40}(e^- + h^+) \rightarrow Bi_2WO_6(h^+) + Bi_{25}FeO_{40}(e^-)Bi_{25}FeO_{40}(e^-) + O_2 \rightarrow Bi_{25}FeO_{40} + {}^{\cdot}O_2^-Bi_2WO_6(h^+) + H_2O \rightarrow {}^{\cdot}OH + Bi_2WO_6Bi_2WO_6(h^+) + {}^{\cdot}O_2^- + {}^{\cdot}OH + MB \rightarrow Bi_2WO_6 + \text{Degradation products}$$

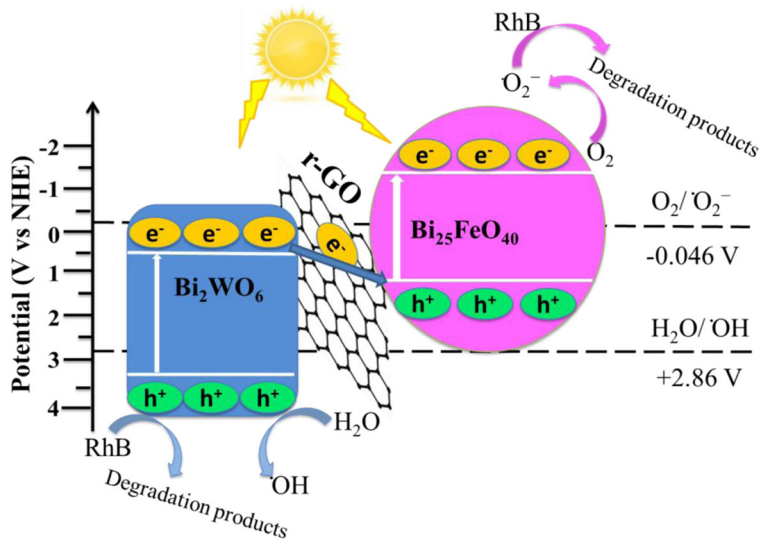

Fig. 12 Z-Scheme charge transfer process in the Bi_2WO_6/r-GO/$Bi_{25}FeO_{40}$ composites

Conclusion

In summary, the Z-scheme Bi_2WO_6/r-GO/$Bi_{25}FeO_{40}$ photocatalyst is successfully prepared by the hydrothermal method, which exhibits high photocatalytic activity in the degradation of MB solution under visible light compared with single Bi_2WO_6 and $Bi_{25}FeO_{40}$. Furthermore, Bi_2WO_6/r-GO/$Bi_{25}FeO_{40}$ still maintains a high degradation rate for MB solution after four consecutive reuses. In this photocatalytic process, the r-GO is regarded as an electron transport bridge that could rapidly accumulate h^+ in VB of Bi_2WO_6 and e^- in CB of $Bi_{25}FeO_{40}$, both of them are the main active substances in dye degradation; therefore, the photocatalytic activity of the ternary composite is improved. We believe this work may provide new insights and perspectives for the preparation of new Z-scheme photocatalysts and be successfully applied in the environmental field.

Compliance with ethical standards

Conflict of interest The authors declare that they have no conflicts of interest.

References

And CZ, Zhu Y (2010) Synthesis of square Bi_2WO_6 nanoplates as high-activity visible-light-driven photocatalysts. Chem Mater 17:3537–3545

Bai Y, Chen T, Wang P, Wang L, Ye L, Shi X, Bai W (2016) Size-dependent role of gold in g-C_3N_4/BiOBr/Au system for photocatalytic CO_2 reduction and dye degradation. Sol Energ Mat Sol C 157:406–414

Basith MA, Ahsan R, Zarin I, Jalil MA (2018) Enhanced photocatalytic dye degradation and hydrogen production ability of $Bi_{25}FeO_{40}$-rGO nanocomposite and mechanism insight. Sci Rep-UK 8:11090

Chen L, He F, Zhao N, Guo R (2017) Fabrication of 3D quasi-hierarchical Z-scheme RGO-Fe_2O_3-MoS_2 nanoheterostructures for highly enhanced visible-light-driven photocatalytic degradation. Appl Surf Sci 420:669–680

de Góis MM, de Paiva Araújo W, da Silva RB, da Luz GE Jr, Soares JM (2019) $Bi_{25}FeO_{40}$-Fe_3O_4-Fe_2O_3 composites: synthesis, structural characterization, magnetic and UV–visible photocatalytic properties. J Alloy Compd 785:598–602

Fu H, Pan C, Yao W, Zhu Y (2005) Visible-light-induced degradation of rhodamine B by nanosized Bi_2WO_6. J Phys Chem B 109:22432–22439

Hou J, Qu Y, Krsmanovic D, Ducati C, Eder D, Kumar RV (2010) Hierarchical assemblies of bismuth titanate complex architectures and their visible-light photocatalytic activities. J Mater Chem 20:2418–2423

Hu X, Liu X, Tian J, Li Y, Cui H (2017) Towards full-spectrum (UV, visible, and near-infrared) photocatalysis: achieving an all-solid-state Z-scheme between Ag_2O and TiO_2 using reduced graphene oxide as the electron mediator. Catal Sci Technol 7:4193–4205

Ji W, Li M, Zhang G, Wang P (2017) Controlled synthesis of $Bi_{25}FeO_{40}$ with different morphologies: growth mechanism and enhanced photo-Fenton catalytic properties. Dalton T 46:10586–10593

Jiang D, Xiao P, Shao L, Li D, Chen M (2017) RGO-promoted all-solid-state g-C_3N_4/$BiVO_4$ Z-scheme heterostructure with enhanced photocatalytic activity toward the degradation of antibiotics. Ind Eng Chem Res 56:8823–8832

Jo WK, Selvam NCS (2017) Z-scheme CdS/g-C_3N_4 composites with RGO as an electron mediator for efficient photocatalytic H_2 production and pollutant degradation. Chem Eng J 317:913–924

Köferstein R, Buttlar T, Ebbinghaus SG (2014) Investigations on $Bi_{25}FeO_{40}$ powders synthesized by hydrothermal and combustion-like processes. J Solid State Chem 217:50–56

Lei GE, Liu J (2011) Efficient visible light-induced photocatalytic degradation of methyl orange by QDs sensitized CdS-Bi_2WO_6. Appl Catal B-Environ 105:289–297

Lei GE, Han C, Jing L (2011) Novel visible light-induced g-C_3N_4/Bi_2WO_6 composite photocatalysts for efficient degradation of methyl orange. Appl Catal B-Environ 108:100–107

Li P, Zhou Y, Li H, Xu Q, Meng X, Wang X, Zou Z (2014) All-solid-state Z-scheme system arrays of Fe_2V4O_{13}/RGO/CdS for visible light-driving photocatalytic CO_2 reduction into renewable hydrocarbon fuel. Chem Commun 51:800–803

Li X, Fang S, Ge L, Han C, Qiu P, Liu W (2015) Synthesis of flower-like Ag/AgCl-Bi_2MoO_6 plasmonic photocatalysts with enhanced visible-light photocatalytic performance. Appl Catal B-Environ 176:62–69

Li Q, Wang F, Hua Y, Luo Y, Liu X, Duan G, Yang X (2017) Deposition-precipitation preparation of Ag/Ag_3PO_4/WO_3 nanocomposites for efficient visible-light degradation of rhodamine B under strongly acidic/alkaline conditions. J Colloid Interf Sci 506:207–216

Lin X, Xu D, Jiang S, Xie F, Song M, Zhai H, Chang L (2017) Graphitic carbon nitride nanocrystals decorated AgVO3 nanowires with enhanced visible-light photocatalytic activity. Catal Commun 89:96–99

Liu T, Li Y, Du Q, Du Q, Sun J, Jiao Y (2012) Adsorption of methylene blue from aqueous solution by grapheme. Colloids Surf B Biointerfaces 90:197–203

López R, Gómez R (2012) Band-gap energy estimation from diffuse reflectance measurements on sol–gel and commercial TiO_2: a comparative study. J Sol-Gel Sci Technol 61:1–7

Ma D, Wu J, Gao M, Xin Y, Ma T, Sun Y (2016) Fabrication of Z-scheme g-C_3N_4/RGO/Bi_2WO_6 photocatalyst with enhanced visible-light photocatalytic activity. Chem Eng J 290:136–146

Miao X, Shen X, Wu J, Ji Z, Wang J, Kong L, Song C (2017) Fabrication of an all solid Z-scheme photocatalyst g-C_3N_4/GO/AgBr with enhanced visible light photocatalytic activity. Appl Catal A-Gen 539:104–113

Rakibuddin M, Mandal S, Ananthakrishnan R (2017) A novel ternary CuO decorated Ag_3AsO_4/GO hybrid as a Z-scheme photocatalyst for enhanced degradation of phenol under visible light. New J Chem 41:1380–1389

Sangeeta A, Do-Heyoung K (2018) Synthesis of Bi_2S_3/Bi_2WO_6 hierarchical microstructures for enhanced visible light driven photocatalytic degradation and photoelectrochemical sensing of ofloxacin. Chem Eng J 354:692–705

Saravanan R, Joicy S, Gupta VK, Narayanan V, Stephen AJMS (2013) Visible light induced degradation of methylene blue using CeO_2/V_2O_5 and CeO_2/CuO catalysts. Mater Sci Eng C 33:4725–4731

Shen H, Wang J, Jiang J, Luo B, Mao B, Shi W (2017) All-solid-state Z-scheme system of RGO-Cu_2O/Bi_2O_3 for tetracycline degradation under visible-light irradiation. Chem Eng J 313: 508–517

Shi Q, Zhao W, Xie L, Chen J, Zhang M, Li Y (2016) Enhanced visible-light driven photocatalytic mineralization of indoor toluene via a $BiVO_4$/reduced graphene oxide/Bi_2O_3 all-solid-state Z-scheme system. J Alloy Compd 662:108–117

Wang G, Cheng D, He T, Hu Y, Deng Q, Mao Y, Wang S (2019) Enhanced visible-light responsive photocatalytic activity of $Bi_{25}FeO_{40}$/$Bi_2Fe_4O_9$ composites and mechanism investigation. J Mater Sci-Mater El 30:1–11

Wisedsri R, Chaisuwan T, Wongkasemjit S (2011) Hierarchical architecture of $Bi_{12}TiO_{20}$ via ethylene glycol-mediated synthesis route. Mater Lett 65:3237–3240

Wu T, Liu G, Zhao J, Hidaka H, Serpone N (1998) Photoassisted degradation of dye pollutants. V. Self-photosensitized oxidative transformation of rhodamine B under visible light irradiation in aqueous TiO_2, dispersions. J Phys Chem B 102: 5845–5851

Wu J, Duan F, Zheng Y, Xie Y (2007) Synthesis of Bi_2WO_6 nanoplate-built hierarchical nest-like structures with visible-light-induced photocatalytic activity. J Phys Chem C 111: 12866–12871

Wu F, Li X, Liu W, Zhang S (2017) Highly enhanced photocatalytic degradation of methylene blue over the indirect all-solid-state Z-scheme g-C_3N_4-RGO-TiO_2 nanoheterojunctions. Appl Surf Sci 405:60–70

Xu CS, Wen TL, Wan ZH, Zhou H, Hao YY, Yi FZ (2015) Enhanced photocatalytic activity of cadmium-doped Bi_2WO_6 nanoparticles under simulated solar light. J Nanopart Res 17:1–10

Xu D, Cheng B, Wang W, Jiang C, Yu J (2018) Ag_2CrO_4/g-C_3N_4/graphene oxide ternary nanocomposite Z-scheme photocatalyst with enhanced CO_2 reduction activity. Appl Catal B-Environ 231:368–380

Zhang L, Wong KH, Chen Z, Jimmy CY, Zhao J, Hu C, Chan CY, Wong PK (2009) AgBr-Ag-Bi_2WO_6 nanojunction system: a novel and efficient photocatalyst with double visible-light active components. Appl Catal A-Gen 363:221–229

Zhang L, Zhang X, Zou Y, Xu YH, Pan CL, Hu JS, Hou CM (2015) Hydrothermal synthesis, influencing factors and excellent photocatalytic performance of novel nanoparticle-assembled $Bi_{25}FeO_{40}$ tetrahedrons. Cryst Eng Comm 17: 6527–6537

Zhang C, Chen G, Li C, Sun J, Lv C, Fan S, Xing W (2016a) In situ fabrication of Bi_2WO_6/MoS_2/RGO heterojunction with nanosized interfacial contact via confined space effect toward enhanced photocatalytic properties. ACS Sustain Chem Eng 4:5936–5942

Zhang L, Zou Y, Song J, Pan CL, Sheng SD, Hou CM (2016b) Enhanced photocatalytic activity of $Bi_{25}FeO_{40}$-Bi_2WO_6 heterostructures based on the rational design of the heterojunction interface. RSC Adv 6:26038–26044

Zhou P, Yu J, Jaroniec M (2014) All-solid-state Z-scheme photocatalytic systems. Adv Mater 26:4920–4935

Zhou YX, Tong L, Zeng XH, Chen XB (2015) Fe_3O_4@Bi_2WO_6 core-shell structured microspheres: facile construction and magnetically recyclable photocatalytic activity under visible-light. J Nanosci Nanotechnol 15(2015):9868–9873

Zhu P, Chen Y, Duan M, Ren Z, Hu M (2018) Construction and mechanism of a highly efficient and stable Z-scheme Ag_3PO_4/reduced graphene oxide/Bi_2MoO_6 visible-light photocatalyst. Catal Sci Technol 8:3818–3832